

Post-Transition Metal Sn-Based Chalcogenide Perovskites: A Promising Lead-Free and Transition Metal Alternative for Stable, High-Performance Photovoltaics

Surajit Adhikari*, Sankhasuvra Das, and Priya Johari*

*Department of Physics, School of Natural Sciences,
Shiv Nadar Institution of Eminence, Greater Noida,
Gautam Buddha Nagar, Uttar Pradesh 201314, India.*

Chalcogenide perovskites (CPs) have emerged as promising materials for optoelectronic applications due to their stability, non-toxicity, small bandgaps, high absorption coefficients, and defect tolerance. Although transition metal-based CPs, particularly those incorporating Zr and Hf, have been well-studied, they often exhibit higher bandgaps, lower charge carrier mobility, and reduced efficiency compared to lead-based halide perovskites (HPs). Tin (Sn), a post-transition metal with a similar oxidation state (+4) as Zr and Hf in ABX_3 structures but with different valence characteristics, remains underexplored in CPs. Given the influence of valence states on material properties, Sn-based CPs are of great interest. This study employs density functional theory (DFT), density functional perturbation theory (DFPT), and many-body perturbation theory (GW and BSE) to investigate a series of distorted Sn-based CPs ($ASnX_3$, $A = Ca, Sr, Ba$; $X = S, Se$). Our results demonstrate that these perovskites are mechanically stable and exhibit lower direct G_0W_0 bandgaps (0.79–1.50 eV) compared to their Zr- and Hf-based counterparts. Analysis of carrier-phonon interactions reveals that the charge-separated polaronic state is less stable than the bound exciton state in these materials. Additionally, polaron-assisted charge carrier mobilities for electrons (21.33–416.02 $cm^2V^{-1}s^{-1}$) and holes (7.02–260.69 $cm^2V^{-1}s^{-1}$) are comparable to or higher than those in lead-based HPs and significantly exceed those of Zr- and Hf-based CPs, owing to reduced carrier-phonon coupling. The estimated spectroscopic limited maximum efficiency (24.2%–31.2%)—confirmed through perovskite solar cell (PSC) simulations using SCAPS-1D software—indicates that these materials are promising candidates for photovoltaic applications. Overall, this study highlights the potential of Sn as a superior alternative to transition metals in CPs, particularly for photovoltaic applications, where smaller electronegativity differences lead to reduced bandgaps and reduced polaronic effects improved charge carrier mobility. These findings are expected to stimulate further experimental investigation into Sn-based CPs.

I. INTRODUCTION:

Chalcogenide perovskites (CPs)[1–4] have recently emerged as a potential alternative for the high-performing inorganic-organic halide perovskites (IOHPs)[5–8]. While IOHPs face significant obstacles for their large-scale industrial applications owing to the toxicity of lead and instability due to the presence of organic cations[9, 10], CPs show promise because of their vast availability in the earth’s crust, non-toxic nature, and exceptional stability[1, 11–13]. In addition to these advantages, CPs exhibit favorable characteristics such as small electronic bandgap, high absorption coefficient, promising defect tolerance, good charge carrier mobility, and excellent power conversion efficiency (PCE)[2–4, 14, 15], which point toward their potential application in a variety of optoelectronic devices.

Similar to the typical three-dimensional halide perovskites (HPs), the chemical formula of chalcogenide perovskites is expressed as ABX_3 [4, 16], where A and B stand for divalent alkali-earth metal cations (Ca^{2+} , Sr^{2+} , Ba^{2+}) and tetravalent transition metal cations (Ti^{4+} , Zr^{4+} , and Hf^{4+}), respectively, and X is typically a chalcogen anion such as S^{2-} or Se^{2-} . Numerous experimental and theoretical investigations have demonstrated the successful synthesis of chalcogenide perovskites and unveiled their intriguing properties[1–4, 11–14, 17, 18]. For example, Lelieveld et al.[17] had synthesized the distorted phase of $CaZrS_3$, $SrZrS_3$, $BaZrS_3$, $CaHfS_3$, $SrHfS_3$, and $BaHfS_3$ in 1980, while later, the needle-like phase[18–20] of $SrZrS_3$, $SrZrSe_3$, and $SrHfSe_3$ CPs were also synthesized by various groups in the end of 20th century and beginning of 21st century. In 2016, Perera et al.[21] used high-temperature sulfurization of the oxides with CS_2 to synthesize $AZrS_3$ ($A = Ba, Ca, and Sr$). On the other hand, in 2015, Sun et al.[4] theoretically affirmed the formation of two distinct phases of CPs at room temperature: the needle-like phase (NH_4CdCl_3 -type) and the distorted phase ($GdFeO_3$ -type), both sharing the orthorhombic structure with same space group $Pnma$ (No. 62), and predicted them to be promising for application in solar cells. In addition, several first-principles DFT-based studies have been conducted, indicating that CPs exhibit interesting electronic and optical properties suitable for use in photovoltaic applications[4, 14–16, 22].

* sa731@snu.edu.in, priya.johari@snu.edu.in

Several studies have primarily focused on Zr ($[\text{Kr}]4d^25s^2$) and Hf ($[\text{Xe}]4f^{14}5d^26s^2$) transition metal-based CPs, where the valence band configurations involve d - and s - orbitals[14, 15, 22]. These materials are demonstrated to exhibit exciton binding energies ranging from 0.02 to 0.26 eV, which are comparable to or higher than those observed in conventional lead-based HPs (0.01–0.10 eV)[23–25]. However, the main drawback of these CPs lies in their reduced charge carrier mobility ($6.84\text{--}77.59\text{ cm}^2\text{V}^{-1}\text{s}^{-1}$) and lower PCE (10.56%–25.02%) compared to conventional HPs, which have charge carrier mobility and PCE in the range of $57\text{--}290\text{ cm}^2\text{V}^{-1}\text{s}^{-1}$ [26, 27] and 21.15%–28.97%[28, 29], respectively. These limitations are majorly due to prominent polaronic effects and relatively higher bandgaps, which hinder their effectiveness for solar cell applications. This makes exploration of alternatives for the B-site cation even more crucial in order to achieve high polaronic charge carrier mobility along with high PCE, thereby enhancing the effectiveness of CPs for solar cell applications.

The polaronic effects are more pronounced in transition metal-based CPs. However, if the post-transition metal Sn ($[\text{Kr}]4d^{10}5s^25p^2$), which also exhibits a +4 oxidation state, is used in place of transition metals like Zr and Hf, the polaronic effects could be mitigated due to different valence states. Additionally, a lower difference in the electronegativity of Sn and X (S, Se) may offer the potential for achieving appropriate bandgaps for photovoltaic applications. Recent first-principles calculations highlight the potential of Sn as a B-site cation *via*. distorted SrSnX_3 (X = S, Se) perovskites as promising photovoltaic materials solely based on their electronic and optical properties up to the HSE06 level[30, 31]. Experimental investigations have substantiated this potential by fabricating distorted CaSnS_3 perovskite at $500\text{Å}^\circ\text{C}$ [32]. Basera et al.[14] have furthermore provided valuable insights into the photovoltaic properties of distorted CaSnS_3 , as well as needle-like phases of BaSnS_3 and SrSnS_3 perovskites. However, the challenge posed by these needle-like CPs lies in their higher bandgap (1.91–2.04 eV) and lower theoretical efficiency (21.80%). In contrast, the bandgap of distorted CaSnS_3 falls within the optimal range at 1.43 eV, with theoretical efficiency reaching up to 32.45%[14]. Motivated by these findings, we aim to conduct a comprehensive theoretical analysis of post-transition metal Sn-based distorted CPs to elucidate their suitable photovoltaic application features.

Henceforth, we have endeavored to meticulously explore the optoelectronic, transport, excitonic, and polaronic properties of distorted Sn-based, ASnX_3 (A = Ca, Sr, Ba; X = S, Se) CPs utilizing a combination of density functional theory (DFT)[33, 34], density functional perturbation theory (DFPT)[35], and advanced many-body perturbation theory based methodologies like GW and BSE[36, 37]. Initially, the crystal structures are optimized using semilocal PBE[38] exchange–correlation (xc) functional, and their stability has been examined. The electronic properties of the relaxed structures are calculated using HSE06[39] xc functional as well as G_0W_0 @PBE[40, 41] methodology. The investigated CPs exhibit direct bandgaps ranging from 0.79 to 1.50 eV, which fall within the similar range to that of conventional lead-based HPs[23, 28] and are lower than the bandgaps observed in Zr- and Hf-based CPs[14, 15, 22]. Following this, optical properties and exciton binding energies (E_B) are determined through the Bethe-Salpeter equation (BSE)[42, 43] method. Furthermore, employing the DFPT technique, the ionic contribution to the dielectric function is computed, and the Fröhlich model is invoked to evaluate polaronic attributes such as carrier-phonon coupling strength and polaron mobility ($21.33\text{--}416.02\text{ cm}^2\text{V}^{-1}\text{s}^{-1}$). Conclusively, the estimation of the spectroscopic limited maximum efficiency (SLME)[44] between 24.20%–31.20% utilizing the quasiparticle (QP) bandgap and absorption coefficient underscores ASnX_3 as a material with significant potential for photovoltaic applications. This has been further confirmed by performing the conventional device (FTO/ TiO_2 / ASnX_3 /Spiro-OMeTAD/Au) simulations using SCAPS-1D software [45–48].

II. COMPUTATIONAL METHODOLOGIES AND NUMERICAL SIMULATIONS:

A. Computational Details:

In this work, the state-of-the-art first-principles calculations based on density functional theory (DFT)[33, 34], density functional perturbation theory (DFPT)[35], and many-body perturbation theory (MBPT)[36, 37] were performed using the Vienna Ab initio Simulation Package (VASP)[49, 50]. In all constituent elements, the valence electrons and atomic core interactions were described using the projector-augmented wave (PAW) pseudopotentials[51]. The PAW pseudopotentials with valence-electron configurations considered for Ca, Sr, Ba, Sn, S, and Se were $3s^23p^64s^2$, $4s^24p^65s^2$, $5s^25p^66s^2$, $4d^{10}5s^25p^2$, $3s^23p^4$, and $4s^24p^4$, respectively. For the structural optimization, the generalized gradient approximation (GGA)[38] based exchange–correlation (xc) functional of Perdew, Burke, and Ernzerhof (PBE) was employed, which takes into account the electron–electron interactions. The plane-wave cutoff energy was set to 400 eV, and the electronic self-consistent-field iteration energy convergence threshold was chosen as 10^{-6} eV. The lattice constants and coordinates of all the atoms were fully optimized until the Hellmann-Feynman forces on each atom were less than 0.01 eV/Å. The Γ -centered $7 \times 7 \times 5$ \mathbf{k} -point sampling was used for Brillouin zone integration in order to determine the optimized structures. Visualization for Electronic and STructural Analysis (VESTA)[52] software package was used to display the optimized crystal structures.

The phonon spectra were calculated using the DFPT method as implemented in the PHONOPY[53] package by considering a $2 \times 2 \times 2$ supercell. Since, GGA is known to underestimate the bandgap, the electronic band structures were computed using the hybrid HSE06[39] xc functional as well as many-body perturbation theory (MBPT) based GW[40, 41] (G_0W_0 @PBE) method. Note that the spin-orbit coupling (SOC) effect was not considered as it does not impact the bandgap (for details, see the Supplemental Material) of the considered systems. The effective mass was computed by SUMO[54] using a parabolic fitting of the band edges. We also carried out Bethe-Salpeter equation (BSE)[42, 43] based calculations on top of the single-shot GW(G_0W_0)@PBE to precisely estimate the optical properties, which takes explicitly into account the electron-hole interaction. Here, a Γ -centered $3 \times 3 \times 2$ \mathbf{k} -grid and a converged 640 NBANDS were used for the GW-BSE calculations. The polarizability calculations were performed using a frequency grid of 60 points to ensure accurate results. In our GW calculations, we used the plasmon-pole approximation (PPA) to model the frequency dependence of the dielectric function (ALGO = GW0). Additionally, the plane-wave cutoff for the response function was set to ENCUTGW = 267 eV (2/3 of ENCUT) for both GW and BSE calculations. The electron-hole kernel for the BSE calculations was generated by considering 24 occupied and 24 unoccupied bands. The VASPKIT[55] package was used to post-process the elastic and optical properties. The ionic contribution to the dielectric constant was also calculated using the DFPT method.

Using the hydrogenic Wannier–Mott (WM)[22, 56] model, the exciton binding energy (E_B) for a screened Coulomb interacting $e - h$ pair is calculated as follows:

$$E_B = \left(\frac{\mu^*}{m_0 \varepsilon_{\text{eff}}^2} \right) R_\infty, \quad (1)$$

where, μ^* represents the reduced mass of the charge carriers, m_0 denotes the rest mass of electron, ε_{eff} is the effective dielectric constant, and R_∞ is the Rydberg constant.

The phonon screening correction to the exciton binding energy (E_B) is given by[57]:

$$\Delta E_B^{ph} = -2\omega_{LO} \left(1 - \frac{\varepsilon_\infty}{\varepsilon_{\text{static}}} \right) \frac{\left(\sqrt{1 + \omega_{LO}/E_B} + 3 \right)}{\left(1 + \sqrt{1 + \omega_{LO}/E_B} \right)^3}, \quad (2)$$

where, ε_∞ and $\varepsilon_{\text{static}}$ are the electronic (optical) and static (electronic + ionic) dielectric constants, and ω_{LO} is the characteristic phonon angular frequency. The thermal "B" approach of Hellwarth et al.[58] is used to determine ω_{LO} by taking the spectral average of the multiple phonon branches (for details, see the Supplemental Material).

Within the framework of Fröhlich's polaron model, the longitudinal optical phonons and the electron traveling through the lattice interact via the dimensionless Fröhlich parameter α , which is expressed as[59],

$$\alpha = \frac{1}{4\pi\varepsilon_0} \frac{1}{2} \left(\frac{1}{\varepsilon_\infty} - \frac{1}{\varepsilon_{\text{static}}} \right) \frac{e^2}{\hbar\omega_{LO}} \left(\frac{2m^*\omega_{LO}}{\hbar} \right)^{1/2}, \quad (3)$$

where ε_0 is the permittivity of free space and m^* is the carrier effective mass. One can also estimate the polaron energy (E_p) by knowing the value of α using equation[14, 22]:

$$E_p = (-\alpha - 0.0123\alpha^2)\hbar\omega_{LO} \quad (4)$$

Feynman's extended version of Fröhlich's polaron theory (for a small α) is also used to obtain the effective mass of the polaron (m_p) as follows[60]:

$$m_p = m^* \left(1 + \frac{\alpha}{6} + \frac{\alpha^2}{40} + \dots \right) \quad (5)$$

Finally, using the Hellwarth polaron model[58], the polaron mobility is defined as follows:

$$\mu_p = \frac{(3\sqrt{\pi}e)}{2\pi c\omega_{LO}m^*\alpha} \frac{\sinh(\beta/2)}{\beta^{5/2}} \frac{w^3}{v^3} \frac{1}{K(a,b)} \quad (6)$$

where e is the charge of the electron, $\beta = \hbar c\omega_{LO}/k_B T$, and w and v are the temperature-dependent variational parameters, and $K(a, b)$ is a function of β , w , and v (for details, see the Supplemental Material).

B. SCAPS-1D Numerical Simulations:

SCAPS-1D software is utilized to conduct numerical device simulations on solar cells to assess their performance and aid in design optimization. The tool was developed by Prof. M. Burgelman at the Department of Electronics and Information Systems (ELIS) of the University of Gent, Belgium[61, 62]. SCAPS solves Poisson's equation, which correlates the electrostatic potential to the overall charge density, along with continuity equations for electrons and holes in the conduction and valence bands, respectively. It can predict device characteristics such as current density-voltage curve, efficiency, energy bands, and other properties of the solar cell structure under illumination. Figure 5(a) shows the proposed perovskite solar cell (PSC) structure having the architecture of FTO/TiO₂/Perovskite/Spiro-OMeTAD/Au. In this proposed structure, Spiro-OMeTAD was used as the hole transport layer (HTL), TiO₂ was used as the electron transport layer (ETL), FTO (fluorine-doped tin oxide) as the transparent conducting oxide (TCO), and perovskite as the absorber layer. Gold (Au), having a work function of 5.1 eV, was employed as the back metallic contact. The simulation parameters for the HTL, ETL, and FTO, chosen based on theoretical and experimental results[45], are listed in Table S15 of the Supplemental Material. Table S16 also shows the input parameters for the perovskite layer, estimated through our theoretical calculations (for details, see the Supplemental Material). The simulations were conducted under the illumination of AM1.5G at 300K working temperature. The Poisson's equation and the continuity equations of both the carriers (electrons and holes) for SCAPS-1D simulation are written as[46, 47],

$$\frac{\partial^2 \psi}{\partial x^2} = -\frac{q}{\varepsilon}[p(x) - n(x) + N_D - N_A + \rho_p \rho_n] \quad (7)$$

$$-\left(\frac{1}{q}\right) \frac{\partial J_p}{\partial x} + G_{op} - R(x) = \frac{\partial p}{\partial t} \quad (8)$$

$$\left(\frac{1}{q}\right) \frac{\partial J_n}{\partial x} + G_{op} - R(x) = \frac{\partial n}{\partial t} \quad (9)$$

Here ψ is the electrostatic potential, ε is the permittivity of the material, p and n are electron and hole concentrations, N_D and N_A are donor and acceptor densities, J_n and J_p are electron and hole current densities, ρ_n and ρ_p are electron and hole distribution, R is the recombination, and G_{op} is the optical generation rate.

The open circuit voltage (V_{oc}) of the perovskite solar cell (PSC) is given by[45],

$$V_{oc} = \frac{nk_B T}{q} \ln\left(\frac{J_{sc}}{J_s} + 1\right) \quad (10)$$

where J_{sc} is the short circuit current density and J_s is the reverse saturation current. The Fill Factor (FF) is given by[48]:

$$FF = \frac{P_{max}}{J_{sc} V_{oc}} \quad (11)$$

and the Power Conversion efficiency, PCE (η) is defined as[48]:

$$\eta = \frac{P_{max}}{P_{in}} = \frac{FF \times J_{sc} \times V_{oc}}{P_{in}} \quad (12)$$

where P_{max} is the maximum power of the solar cell, and P_{in} is the input solar power equivalent to the AM1.5G Sun spectrum.

III. RESULTS AND DISCUSSIONS:

In this study, we undertook a systematic and thorough investigation into the distorted phases of post-transition metal Sn-based chalcogenide perovskites ASnX₃ (A = Ca, Sr, Ba; X = S, Se) to explore their potential optoelectronic features. The subsequent sections delve into the stability as well as the structural, electronic properties, transport phenomena, optical properties, excitonic dynamics, polaronic effects, and the spectroscopic limited maximum efficiency (SLME) of ASnX₃ chalcogenide perovskites. This detailed examination and discussion aims to establish a foundational understanding and provide insights to guide future experimental endeavors.

A. Structural Properties:

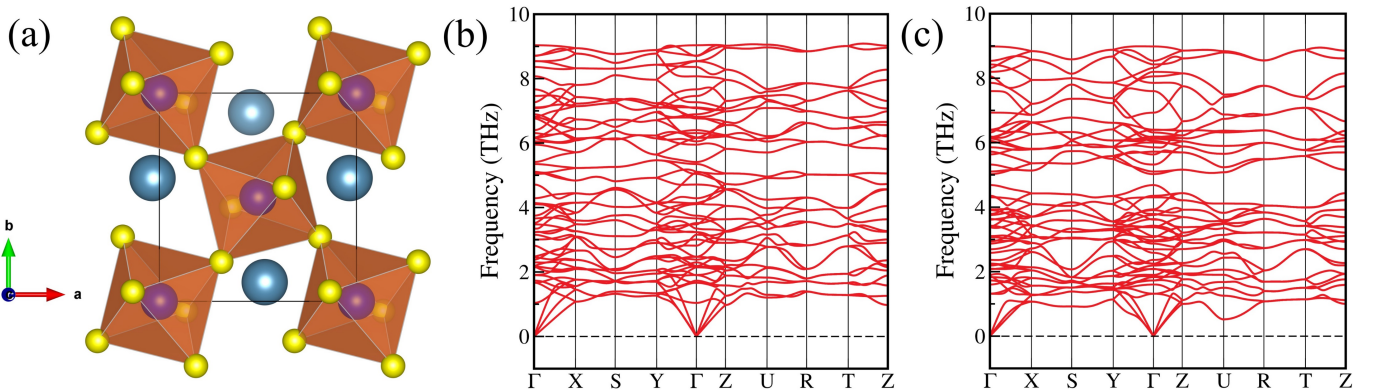


Figure 1. (a) Crystal structure of CaSnS_3 in orthorhombic distorted phase, and phonon dispersion curves of (b) SrSnS_3 , and (c) BaSnS_3 calculated using DFPT method. Blue, purple, and yellow balls represent Ca, Sn, and S atoms, respectively.

The orthorhombic distorted crystal structure with the space group $Pnma$ (No. 62)[17] of chalcogenide perovskites ASnX_3 ($A = \text{Ca, Sr, Ba}$; $X = \text{S, Se}$) are presented in Figure 1(a) and Figure S1. The crystal structure of these compounds usually consists of four formula units, i.e., 20 atoms, of which 4 are Ca/Sr/Ba, 4 are Sn, and 12 are S or Se atoms. In this distorted phase, the alkaline earth elements (A-site cations) have 12-fold coordination, and they form cuboctahedrons with chalcogenides X (S or Se). On the other hand, the corner-sharing distorted octahedrons $[\text{SnX}_6]^{8-}$ are produced due to the 6-fold coordination of Sn cation with X (S or Se) atoms in a distorted and tilted way. The lattice parameters of the optimized crystal structures are calculated using the PBE xc functional and are tabulated in Table I. It is found that the lattice parameters are in good agreement with previous theoretical and available experimental results[30, 32]. However, for CaSnS_3 , there is a discrepancy in the c-lattice constant between the theoretical and experimental values, which could influence the bandgap, as variations in bond lengths and angles modify the electronic band dispersion. In addition, Table S1 presents detailed information on the octahedral distortions of SnX_6 octahedra in ASnX_3 ($A = \text{Ca, Sr, Ba}$; $X = \text{S, Se}$) CPs, including parameters such as average bond length, bond angle variance, polyhedral volume, and distortion index. The results indicate that the SnX_6 octahedra in BaSnX_3 ($X = \text{S, Se}$) undergo greater lattice distortion than those in other compounds, likely due to the larger ionic radius of Ba^{2+} , which influences the local bonding environment around the octahedra.

The crystallographic stability of these CPs is quantitatively identified by calculating the Goldschmidt tolerance factor (t), the octahedral factor (μ), and the new tolerance factor (τ)[56, 63, 64] (for details, see the Supplemental Material). From Table S2, it can be noticed that the t , μ , and τ values of these investigated CPs are in the range of 0.879–0.964, 0.348–0.375, and 4.174–4.721, respectively, confirming the reasonable structural stability of these distorted CPs[16, 63]. Furthermore, the decomposition energy is also calculated for these materials using the PBE xc functional to ascertain their thermodynamic stability (for details, see Table S3 of the Supplemental Material). The negative decomposition energy reveals these perovskites to be unstable at 0 K. Still, there remains a possibility for them to stabilize at higher temperatures, as also demonstrated by Hamza et al. by synthesizing CaSnS_3 perovskite at 500° C[32], which is an indicator of their higher temperature stability. Further, the dynamical and mechanical stability of the studied CPs are examined.

Table I. Calculated lattice parameters of ASnX_3 ($A = \text{Ca, Sr, Ba}$; $X = \text{S, Se}$) chalcogenide perovskites.

Configurations	This Work			Previous Work			Reference
	a (Å)	b (Å)	c (Å)	a (Å)	b (Å)	c (Å)	
CaSnS_3	6.71	7.08	9.67	6.69	7.08	11.29	Expt.[32]
SrSnS_3	6.90	7.22	9.82	6.90	7.21	9.84	Theo.[30]
BaSnS_3	7.04	7.27	10.17				
CaSnSe_3	7.06	7.47	10.15				
SrSnSe_3	7.24	7.62	10.29	7.25	7.61	10.31	Theo.[30]
BaSnSe_3	7.32	7.73	10.63				

In Figure 1(b)-(c), the phonon spectra of SrSnS_3 and BaSnS_3 CPs have been depicted, which validates their dynamical stability at 0 K. The rest of the compounds are found to be unstable at 0 K, but they may become

dynamically stable at higher temperatures, as discussed before. To investigate the mechanical stability, the second-order elastic coefficients (C_{ij}) of these CPs are calculated using the energy-strain approach[65] (for details, see the Supplemental Material). The computed C_{ij} values of these compounds are listed in Table S4, and they are found to satisfy the Born stability criteria[65]. Using these elastic coefficients, the bulk modulus (B), shear modulus (G), Young's modulus (Y), and Poisson's ratio (ν) of these materials[66, 67] are investigated (for details, see the Supplemental Material). The fragility of the materials is studied in terms of Pugh's suggested ratio (B/G)[68] and Poisson's ratio (ν). The calculated values of B/G (> 1.75) and ν (> 0.26) reveal that the examined CPs are ductile in nature (see Table S4). Additionally, the longitudinal (v_l), transverse (v_t), and average (v_m) elastic wave velocities and the Debye temperature (Θ_D)[69] are calculated (see Table S5), as they hold crucial significance for flexible optoelectronic applications.

Table II. Bandgap (in eV) of chalcogenide perovskites. Here, Ca- and Sr-based CPs are direct bandgap materials, whereas Ba-based CPs are indirect bandgap materials. For Ba-based CPs, i and d represent indirect and direct bandgaps, respectively.

Configurations	PBE	HSE06	$G_0W_0@PBE$	Previous Work
CaSnS ₃	0.77	1.40	1.44	1.72 (Expt.[32])
SrSnS ₃	0.83	1.45	1.50	1.56 (Theo.[31])
BaSnS ₃	0.64 ^{<i>i</i>} (0.66 ^{<i>d</i>})	1.16 ^{<i>i</i>} (1.23 ^{<i>d</i>})	1.18 ^{<i>i</i>} (1.28 ^{<i>d</i>})	
CaSnSe ₃	0.25	0.70	0.79	
SrSnSe ₃	0.42	0.86	0.88	1.00 (Theo.[31])
BaSnSe ₃	0.54 ^{<i>i</i>} (0.55 ^{<i>d</i>})	0.93 ^{<i>i</i>} (1.00 ^{<i>d</i>})	0.99 ^{<i>i</i>} (1.04 ^{<i>d</i>})	

B. Electronic Properties:

After examining the stability, the electronic properties, such as band structure and partial density of states (PDOS) of the chalcogenide perovskites $ASnX_3$ ($A = \text{Ca, Sr, Ba}$; $X = \text{S, Se}$) are computed to gain deep insights for designing the photoelectric devices. At first, the electronic band structure calculations are performed using the semi-local GGA-PBE xc functional with and without including the spin-orbit coupling (SOC) for these CPs. It is found that GGA-PBE xc functional is unable to predict the correct bandgaps due to the self-interaction error of the electrons (see Table II), and SOC does not have any impact on the bandgap (see Table S6 of the Supplemental Material), which is expected for chalcogenide perovskites[14, 22]. After that, we employed the hybrid HSE06 xc functional and many-body perturbation theory (MBPT) based GW ($G_0W_0@PBE$) method to calculate the bandgaps more accurately. The HSE06 and $G_0W_0@PBE$ calculated band structures of these compounds are depicted in Figure 2 and Figure S3, respectively. Our results revealed that Ca- and Sr-based compounds have direct bandgaps at Γ (0, 0, 0) point, while Ba-based CPs exhibit indirect bandgaps. In the case of BaSnS₃ and BaSnSe₃, the valence band maxima (VBM) are situated at the S (0.5, 0.5, 0) and U (0.5, 0, 0.5) points of the Brillouin zone (BZ), respectively, while the conduction band minima (CBM) are found in between Γ and X (0.5, 0, 0) point for both cases (see Figure 2). Also, both of them exhibit the lowest direct bandgap in between Γ and X point of the BZ. The HSE06 as well as $G_0W_0@PBE$ estimated bandgaps of these CPs are listed in Table II, which closely match with earlier theoretical findings. It is well known that the $G_0W_0@PBE$ method provides highly accurate bandgap values for CPs, yielding results that closely match experimental values[14, 15, 22]. However, the $G_0W_0@PBE$ bandgap of CaSnS₃ (1.44 eV) is in reasonable agreement with its experimental bandgap of 1.72 eV[32], showing a difference of 0.28 eV. The underestimation of the GW bandgap may partly arise from structural discrepancies (c-lattice constant), as GW calculations are sensitive to input geometries, and deviations from experimental structures can affect electronic properties. Additionally, the experimental bandgap of CaSnS₃ was measured at 500 $\text{\AA}^\circ\text{C}$ (773.15 K), while theoretical calculations are performed at 0 K, and this temperature difference could also contribute to the discrepancy. Furthermore, incorporating excitonic effects into the calculations could potentially lead to a larger difference between the theoretical (optical) and experimental bandgaps. The HSE06 and $G_0W_0@PBE$ computed bandgap of these CPs lie in the range of 0.70–1.45 eV and 0.79–1.50 eV, respectively. Thus, the bandgaps of the investigated post-transition metal Sn-based CPs fall within the optimal range for photovoltaic applications, aligning closely with those of conventional APbI₃ ($A = \text{Cs, CH}_3\text{NH}_3$) HPs (1.50–1.85 eV)[23, 28] and being lower than the bandgaps of transition metal based CPs (1.69–2.46 eV)[14, 15, 22] (for details, see Table S14 of the Supplemental Material). This suggests their high suitability for photovoltaic applications.

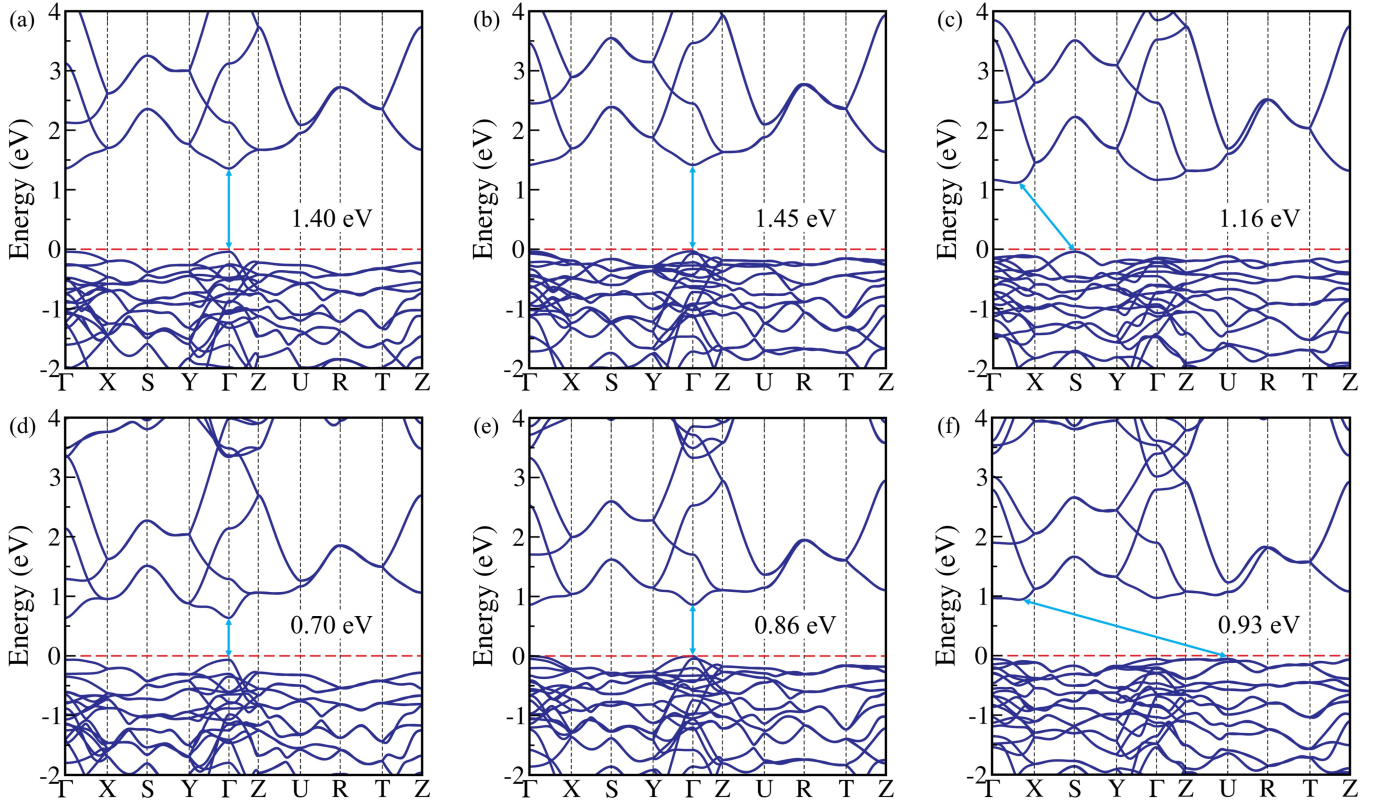


Figure 2. Electronic band structures of (a) CaSnS_3 , (b) SrSnS_3 , (c) BaSnS_3 , (d) CaSnSe_3 , (e) SrSnSe_3 , and (f) BaSnSe_3 chalcogenide perovskites, obtained using the HSE06 xc functional. The Fermi level is set to be zero and marked by the dashed line.

Figure S4 shows the partial density of states (PDOS) and the total density of states (TDOS) for all the studied compounds obtained using the HSE06 xc functional. In ASnS_3 ($A = \text{Ca}, \text{Sr}, \text{Ba}$) CPs, S-3*p* orbitals mainly contribute to the VBM, while the hybridization (sp^3 -type) of S-3*p* and Sn-5*s* orbitals dominates the CBM. Similarly, for ASnSe_3 perovskites, the VBM is primarily contributed by Se-4*p* orbitals, whereas CBM mainly consists of hybridized Se-4*p* and Sn-5*s* orbitals. The hybridization of Se-4*p* and Sn-5*s* orbitals in ASnSe_3 is stronger than the hybridization of S-3*p* and Sn-5*s* orbitals in ASnS_3 , which is mainly responsible for lowering the bandgap in the case of ASnSe_3 as compared to their sulfur counterparts ASnS_3 . On the other hand, in the case of transition metal-based CPs, the bonding (sp^3d^2) is a mix of σ -bonding (from the covalent overlap of orbitals) and π -bonding (to a lesser extent, from *d*-orbital interactions), leading to strong covalent interactions. At the same time, a more significant difference in the electronegativity of Zr/Hf and S/Se adds some ionic characteristics (see Figure S5), which eventually results in more localized electronic states around the atom and, thus, larger bandgaps than Sn-based CPs[14, 15, 22].

Notably, perovskites are highly recognized materials for efficiently transporting charge carriers (electrons and holes). Therefore, in addition to their band structures, we also calculate the corresponding electron (m_e^*) and hole (m_h^*) effective masses by utilizing the fitted E - k dispersion band diagram of G_0W_0 @PBE band structures (Figure S3), employing the formula, $m^* = \hbar^2 [\partial^2 E(k)/\partial k^2]^{-1}$ (for details, see the Supplemental Material). From Table III, it is observed that $m_e^* < 1$, $m_h^* < 1.5$ for all the cases, indicating high carrier mobility and thus better charge carrier transport. Since BaSnX_3 ($X = \text{S}, \text{Se}$) exhibits an indirect bandgap, the effective masses for these compounds are calculated at both their indirect and direct band edges. Also, Table III suggests that Ca- and Sr-based CPs have a high potential for exhibiting ambipolar characteristics.

Table III. Effective mass of electron (m_e^*) and hole (m_h^*) and their reduced mass (μ^*), obtained using the $G_0W_0@PBE$ method. All values are in terms of free-electron mass (m_0) and the bold values provided in parentheses are the effective mass and respective reduced mass at direct band edge.

Configurations	$m_e^* (m_0)$	$m_h^* (m_0)$	$\mu^* (m_0)$
CaSnS ₃	0.403	0.537	0.230
SrSnS ₃	0.608	0.673	0.319
BaSnS ₃	0.674 (0.674)	1.287 (1.121)	0.442 (0.421)
CaSnSe ₃	0.149	0.207	0.087
SrSnSe ₃	0.240	0.385	0.148
BaSnSe ₃	0.717 (0.717)	1.059 (1.237)	0.428 (0.454)

C. Optical Properties:

In addition to the electronic bandgaps, we also explore the optical bandgaps to gain a holistic understanding of the excitonic effects in perovskite materials. These effects, arising from the interaction of electrons and holes, are pivotal for determining the efficiency of light-matter interactions in optoelectronic applications. The above study shows that the electronic properties of these CPs can be well-described by the HSE06 functional. Nevertheless, this functional is known to predict the optical features of these systems with less accuracy. Thus, we performed MBPT-based GW-BSE calculations to calculate the optical properties. In essence, GW calculations compute the fundamental bandgap, which is thought to be more accurate and comparable to photoelectron spectroscopy (PES) and inverse photoelectron spectroscopy (IPES)[40, 41]. In contrast, BSE calculations predict the optical bandgap similar to experimental optical absorption spectroscopy[42, 43].

To evaluate the optical responses of the $ASnX_3$ CPs, BSE calculations are performed on top of the single-shot $GW(G_0W_0)@PBE$, which explicitly considers the electron-hole interaction. The real [$\text{Re}(\epsilon_e)$] and imaginary [$\text{Im}(\epsilon_e)$] part of the frequency-dependent electronic dielectric function calculated using $BSE@G_0W_0@PBE$ are shown in Figure 3. It is discovered that the absorption onset and the first peak position or optical bandgap (E_o) gradually red shift from sulfide (S) to selenide (Se) containing CPs akin to the drop of quasiparticle (QP) bandgap of them (see Table II). For example, the optical bandgap for CaSnS₃ is observed at 1.23 eV, and it shifts to 0.74 eV for CaSnSe₃. After incorporating the excitonic effect in CaSnS₃, it is evident that the difference between the theoretical (optical) bandgap and the experimental bandgap increases by 0.49 eV. However, the underlying reason for this difference remains consistent with the previously discussed influence of structural geometry and temperature. The value of E_o for these $ASnX_3$ CPs falls within the range of 0.74 to 1.26 eV and shifts with the change of the A atom, similar to the variation observed in their QP bandgap (see Table IV). Our calculations reveal that the optical bandgaps of these CPs are consistently smaller than their electronic bandgaps due to significant excitonic effects. This study primarily focuses on the bright excitonic states, however, dark excitons can significantly influence the optical properties of semiconductors, particularly in systems with low symmetry or strong spin-orbit coupling. Dark excitons, which are optically inactive due to spin-forbidden transitions or momentum mismatch, are typically found below the bright excitons in the absorption spectrum. Although they do not couple directly to light, their presence can affect the overall photophysical behavior, such as photoluminescence and carrier dynamics. Nevertheless, an analysis of the BSE eigenvalues revealed no evidence of dark excitons (optically inactive states) below the first bright exciton for the investigated materials.

The electronic dielectric constants (ϵ_∞), which are obtained from the real part of the dielectric function, are also found to be increased from S to Se containing CPs, indicating low charge carrier recombination rate and improved optoelectronic efficiency for the latter[70] (see Table IV). For instance, ϵ_∞ for CaSnS₃ is 7.47, and it increases to 15.15 for CaSnSe₃. Overall, these results reveal that CaSnS₃, SrSnS₃, BaSnS₃, and BaSnSe₃ could be the best choice for photovoltaic applications.

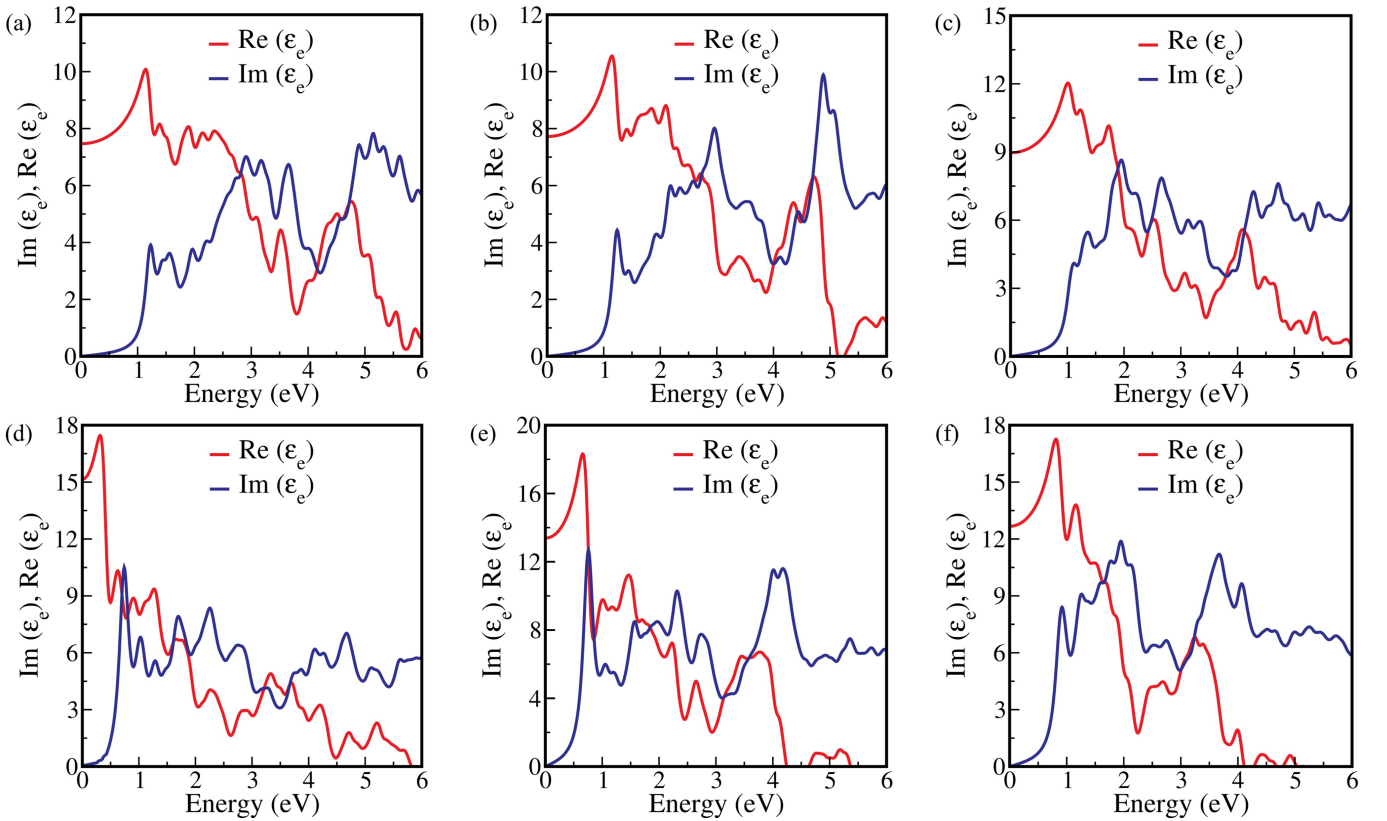


Figure 3. Computed real $[Re(\epsilon_e)]$ and imaginary $[Im(\epsilon_e)]$ part of the electronic dielectric function for (a) $CaSnS_3$, (b) $SrSnS_3$, (c) $BaSnS_3$, (d) $CaSnSe_3$, (e) $SrSnSe_3$, and (f) $BaSnSe_3$ chalcogenide perovskites, obtained using the BSE@ G_0W_0 @ PBE method.

The absorption coefficient $[\alpha(\omega)]$ of a material is a measurable parameter that indicates how many photons (of a specific wavelength) may enter the material before being absorbed. Thus, this descriptor is also essential for photovoltaic applications and offers crucial information regarding the ideal solar energy conversion efficiency. $\alpha(\omega)$ is associated with the dielectric function and can be computed with the following formula[35]:

$$\alpha(\omega) = \sqrt{2}\omega \left[\sqrt{(Re(\epsilon_e))^2 + (Im(\epsilon_e))^2} - Re(\epsilon_e) \right]^{1/2}. \quad (13)$$

Our results from the BSE@ G_0W_0 @ PBE calculation (see Figure S6) imply that all the investigated $ASnX_3$ CPs exhibit high optical absorption coefficients ($\sim 10^4 - 10^5 \text{ cm}^{-1}$), which is desirable for the photovoltaic applications.

D. Excitonic Properties:

In optoelectronic materials, exciton generation plays a significant role in the charge separation properties. For this reason, excitonic parameters, such as exciton binding energy (E_B) and exciton lifetime (τ_{exc}), are crucial descriptors in their applications. The energy required to dissociate an exciton into a single electron (e) and hole (h) pair is known as the exciton binding energy. The GW-calculated electronic gaps are complemented by BSE-computed optical gaps to account for excitonic binding energies. This combined approach allows us to predict material properties with high accuracy, ensuring their relevance for practical device design. Theoretically, E_B is computed as the difference of the QP bandgap (direct G_0W_0 @PBE bandgap, E_g^d) and the optical bandgap (BSE@ G_0W_0 @PBE peak position, E_o)[56, 71–73], which are tabulated in Table IV. It should be noted that the electronic contribution of the dielectric screening is dominant over the ionic one if E_B is significantly greater than the longitudinal optical phonon energy ($\hbar\omega_{LO}$). In that scenario, one can neglect the ionic contribution, and consequently, E_B remains unchanged[74, 75]. From Table IV and Table VI, it is found that $E_B \gg \hbar\omega_{LO}$ for $ASnX_3$ CPs; therefore, ionic screening to the dielectric function can be disregarded. The E_B values obtained from standard first-principles GW-BSE calculations are found in the range of 0.05–0.24 eV, which are comparable to that of transition metal-based traditional CPs (0.02–0.26

eV)[14, 15, 22] but a little higher than those observed in conventional lead-based HPs (0.01–0.10 eV)[23–25] (for details, see Table S14 of the Supplemental Material). The E_B values obtained from our GW-BSE calculations indicate relatively strong excitonic effects in these materials. While this range may appear too high for direct photovoltaic applications, it is worth noting that these values represent intrinsic properties of isolated bulk materials. In practical device architectures, factors such as dielectric screening from surrounding layers, nanostructuring, or heterostructures can significantly reduce the effective E_B , potentially bringing it within the desired range for photovoltaic applications. Furthermore, these materials may be more suited for other optoelectronic applications, such as light-emitting diodes, photodetectors, or excitonic solar cells, where stronger excitonic effects are advantageous. Here, CaSnSe_3 exhibits the lowest E_B value, attributed to its higher electronic dielectric constant (ϵ_∞), which reduces the Coulomb interaction between the electron and hole.

Table IV. Calculated excitonic parameters for chalcogenide perovskites. Here, E_g^d represents the direct G_0W_0 @PBE bandgap, E_{exc} represents the optical bandgap, E_B represents the exciton binding energy, T_{exc} represents the excitonic temperature, r_{exc} is the exciton radius, $|\phi_n(0)|^2$ is the probability of a wave function at zero separation, ϵ_∞ is the electronic dielectric constant, ϵ_{static} is the static dielectric constant, E_{Bu} and E_{Bl} are the upper and lower bounds of the exciton binding energy, respectively.

Configurations	First-principles method (GW-BSE)						Wannier–Mott model			
	E_g^d (eV)	E_o (eV)	E_B (eV)	T_{exc} (K)	r_{exc} (nm)	$ \phi_n(0) ^2$ ($10^{26}m^{-3}$)	ϵ_∞	E_{Bu} (meV)	ϵ_{static}	E_{Bl} (meV)
CaSnS_3	1.44	1.23	0.21	2435	1.72	0.63	7.47	56.06	34.70	2.60
SrSnS_3	1.50	1.26	0.24	2783	1.28	1.52	7.72	72.79	32.55	4.09
BaSnS_3	1.28	1.12	0.16	1855	1.13	2.21	8.97	71.16	45.61	2.75
CaSnSe_3	0.79	0.74	0.05	580	9.21	0.004	15.15	5.16	70.08	0.24
SrSnSe_3	0.88	0.78	0.10	1159	4.79	0.03	13.39	11.23	56.98	0.62
BaSnSe_3	1.04	0.91	0.13	1507	1.48	0.99	12.67	38.46	44.66	3.10

In addition, we have validated the E_B using the Wannier-Mott method[22, 56] through the Eq. 1. This method helps establish a qualitative understanding of excitonic properties and their dependence on effective masses and dielectric screening, serving as a sanity check for trends observed in the ab initio BSE calculations. The Wannier-Mott model is traditionally more applicable to direct bandgap materials. However, for indirect bandgap materials in our study, the effective masses and, subsequently, the reduced masses are calculated at their direct band edges (for details, see table III). Here, ϵ_{eff} lies in between optical (ϵ_∞) and static (ϵ_{static}) dielectric constant. The optical or electronic dielectric constants (ϵ_∞) at the zero frequency limit are obtained using the BSE method. Subsequently, the DFPT calculations are performed to compute the ionic contribution to the dielectric function (ϵ_{ion}), and therefore, the static dielectric constant is calculated as, $\epsilon_{static} = (\epsilon_\infty + \epsilon_{ion})$. In our study, the upper (E_{Bu}) and lower (E_{Bl}) bounds of exciton binding energy are estimated based on the ϵ_∞ and ϵ_{static} , respectively (see Table IV). The upper bound values are smaller but align more closely with the E_B calculated using the GW-BSE method than the lower bound values; however, the overall trend remains consistent. This suggests that in chalcogenide perovskites, the electronic contribution to dielectric screening is more prominent than the ionic contribution.

Furthermore, additional investigations into the ionic (phonon) contribution to the exciton binding energy (E_B) are conducted for the examined CPs. This is because the standard BSE approach within an ab initio framework captures only static screening from electrons to calculate the exciton binding energy. However, it's noteworthy that dynamic electron-electron interactions or electron-phonon coupling may play a crucial role in certain materials, particularly those with significant electron-phonon interactions or where phonons significantly influence optoelectronic properties. Filip and collaborators[57] have recently broadened the discussion to incorporate phonon screening into the analysis of exciton binding energy using equation 2. They achieved this by considering four specific material parameters: reduced effective mass, static and optical dielectric constants, and the frequency of the longitudinal optical phonon mode (ω_{LO}), while assuming isotropic and parabolic electronic band dispersion. Table V indicates that phonon screening leads to a reduction in the E_B ranging from 5.58% to 17.87%, with the modified E_B values ranging from 0.04 to 0.23 eV. While phonon screening does decrease the exciton binding energy, the reduction is not particularly substantial, except in the case of CaSnSe_3 . This also suggests that in most chalcogenide perovskites, the electronic contribution to dielectric screening outweighs the ionic (or phonon) contribution.

Table V. Calculated exciton binding energy (E_B), phonon screening corrections (ΔE_B^{ph}), percentage of phonon screening contribution to the reduction of exciton binding energy (%), and corrected values of exciton binding energy ($E_B + \Delta E_B^{ph}$) for chalcogenide perovskites.

Configurations	E_B (meV)	ΔE_B^{ph} (meV)	Reduction of E_B (%)	$(E_B + \Delta E_B^{ph})$ (meV)
CaSnS ₃	210	-14.68	6.99	195.32
SrSnS ₃	240	-13.39	5.58	226.61
BaSnS ₃	160	-12.42	7.76	147.58
CaSnSe ₃	50	-8.93	17.87	41.07
SrSnSe ₃	100	-8.17	8.17	91.83
BaSnSe ₃	130	-8.08	6.22	121.92

Several excitonic parameters, including excitonic temperature (T_{exc}), exciton radius (r_{exc}), and probability of wave function ($|\phi_n(0)|^2$) for $e-h$ pair at zero separation are also computed using the above quantities (E_B , ε_∞ , and μ^*) to have a definitive estimation of the excitonic properties (for details, see the Supplemental Material). Based on the analysis of exciton radius (r_{exc}), it is observed that in all investigated materials, the electron-hole pairs are distributed over multiple lattice constants, supporting the applicability of the Wannier-Mott model. The inverse of $|\phi_n(0)|^2$ can be used to qualitatively characterize the exciton lifetime (τ_{exc}), which is listed in Table IV (for details, see the Supplemental Material). Consequently, the τ_{exc} values for the investigated CPs are in the order CaSnSe₃ > SrSnSe₃ > CaSnS₃ > BaSnSe₃ > SrSnS₃ > BaSnS₃. For efficient photo-conversion in solar cells, the exciton lifetime (τ_{exc}) should be sufficiently high to extract photo-generated charge carriers before recombination occurs. A longer exciton lifetime corresponds to a lower carrier recombination rate, which enhances the quantum yield and conversion efficiency. Overall, these properties significantly enhance the efficiency of ASnX₃ CPs, making them promising for potential optoelectronic applications.

E. Polaronic Properties:

In polar semiconductors, such as halide perovskite and its derivatives, the scattering mechanism near room temperature is dominant due to the interaction between charge carriers and the macroscopic electric field produced by longitudinal optical phonon (LO)[59]. This interaction strongly influences charge carrier mobility of the system and is anticipated to be the same for the materials of our interest[14, 22]. Therefore, the Fröhlich mesoscopic model[26, 59, 76] is used to describe this interaction and defined by the dimensionless Fröhlich parameter α using Eq. 3. The calculated values of α related to Fröhlich interaction for electrons and holes are given in Table VI and Table S12, respectively. Strong electron (hole)-phonon coupling is indicated by $\alpha > 10$, while $\alpha \ll 1$ often suggests weak coupling[26]. Our results show that the value of α for ASnX₃ CPs lies in the range of 0.64–2.92, suggesting weak to intermediate electron (hole)-phonon coupling for the investigated systems. Additionally, it has been observed that Sn-based CPs exhibit less pronounced polaronic effects compared to transition metal-based CPs[14, 15, 22]. This weaker electron-phonon coupling can be attributed to a lower electron effective mass and a higher electronic dielectric constant, while stronger coupling in transition metal-based CPs results from the opposite factors. Here, CaSnSe₃ exhibits smaller electron-phonon coupling, while BaSnS₃ demonstrates larger electron-phonon coupling for the same reasons. In this context, the specific free volume of these CPs is also evaluated to obtain a qualitative knowledge of the strength of electron-phonon coupling (for details, see the Supplemental Material).

Notably, polaron formation can lead to a decrease in the electron and hole QP energies. This polaron energy (E_p) can also be calculated using α by using Eq. 4. The QP gap, which results from the polaron energy for electrons and holes, is reduced by 76.37, 81.16, 85.32, 18.58, 25.37, and 43.65 meV for CaSnS₃, SrSnS₃, BaSnS₃, CaSnSe₃, SrSnSe₃, and BaSnSe₃, respectively. Comparing the values of E_B from Table IV with the QP gap, it is evident that the energy of charge-separated polaronic states is lower than that of the bound exciton states. This suggests that the charge-separated polaronic states are less stable than the bound excitons.

The other parameters for the polarons, i.e., polaron mass (m_p) and polaron mobility (μ_p), are also estimated using Eq. 5 and Eq. 6, respectively. These parameter values are listed in Table VI and Table S12 for electrons and holes, respectively. One can confirm the enhanced carrier-lattice interactions by higher m_p values, and for this case, the charge carrier mobility decreases than the non-polar or less polar compounds. For example, Ca- and Sr-based compounds exhibit weaker carrier (electron)-lattice interactions compared to Ba-based compounds, resulting in higher mobility for Ca- and Sr-based materials. Also, CaSnSe₃ CP exhibits the highest polaron mobility for electrons, which is obvious due to weak electron-phonon coupling ($\alpha = 0.64$). Overall, these post-transition metal Sn-based CPs are shown to have ambipolar properties and much-improved polaron mobility for electrons (21.33–416.02 cm²V⁻¹s⁻¹) and holes (7.02–260.69 cm²V⁻¹s⁻¹, see Table S12 of the Supplemental Material) than the conventional lead-based

HPs ($57\text{--}290\text{ cm}^2\text{V}^{-1}\text{s}^{-1}$ for electrons and $97\text{--}230\text{ cm}^2\text{V}^{-1}\text{s}^{-1}$ for holes, respectively)[26, 27] as well as transition metal (Zr and Hf) based traditional CPs ($6.84\text{--}77.59\text{ cm}^2\text{V}^{-1}\text{s}^{-1}$ for electrons and $3.76\text{--}100.49\text{ cm}^2\text{V}^{-1}\text{s}^{-1}$ for holes, respectively)[14, 15, 22]. The higher polaron mobility in Sn-based CPs is attributed to less prominent polaronic effects than conventional lead-based HPs and transition metal-based CPs.

Table VI. Calculated polaron parameters for electrons in chalcogenide perovskites. Here, ω_{LO} represents the characteristic phonon angular frequency, θ_D represents the Debye temperature, α represents the Fröhlich interaction parameter, E_p represents the polaron energy, m_p represents the effective mass of the polaron, and μ_p represents the polaron mobility, respectively.

Configurations	ω_{LO} (THz)	θ_D (K)	α	E_p (meV)	m_p/m^*	μ_p ($\text{cm}^2\text{V}^{-1}\text{s}^{-1}$)
CaSnS ₃	4.78	229.51	1.75	35.39	1.37	42.29
SrSnS ₃	4.44	213.18	2.10	39.61	1.46	22.64
BaSnS ₃	3.97	190.62	2.11	35.59	1.46	21.33
CaSnSe ₃	3.20	153.65	0.64	8.55	1.12	416.02
SrSnSe ₃	2.76	132.52	0.97	11.22	1.18	173.92
BaSnSe ₃	2.88	138.28	1.62	19.71	1.33	32.86

F. Spectroscopic Limited Maximum Efficiency:

The above-discussed properties indicate that the investigated systems hold great potential for photovoltaic applications, and to validate this, we also calculated their power conversion efficiency (PCE). The theoretical PCE of each system is calculated using the spectroscopic limited maximum efficiency (SLME) method. SLME was introduced by Yu and Zunger[44] (for details, see the Supplemental Material), which is an improved version of the Shockley-Queisser (SQ) limit[77]. The latter is less realistic since it disregards the losses resulting from radiative recombinations due to the non-conservation of the absorbed photon momentum. SLME incorporates the magnitude of the bandgap and its nature (direct or indirect), the shape of absorption spectra, the thickness of the absorber layer, the material-dependent non-radiative recombination losses, and the temperature. The standard solar spectrum (AM-1.5G), the absorption coefficient, thickness, and the electronic G_0W_0 @PBE bandgap are thus used as inputs to evaluate the theoretical SLME of ASnX_3 ($A = \text{Ca, Sr, Ba}$; $X = \text{S, Se}$) CPs at 293.15 K temperature.

In addition, the optical transition possibility from VBM to CBM for these CPs has been confirmed through the computation of transition dipole moment matrix (P) elements; its square (P^2) gives the transition probability between the initial (VBM) and the final (CBM) state. Figure 4(a) shows the optically allowed dipole transition at Γ -point for CaSnS₃, and for other configurations, see Figure S7. Despite having an indirect electronic bandgap, BaSnS₃ and BaSnSe₃ exhibit an optically allowed dipole transition at their direct band edge. However, when E_g^{da} is not the minimum bandgap of the materials (i.e., $E_g \neq E_g^{da}$), non-radiative recombination plays a vital role in the SLME calculation and the radiative recombinations vary with a factor $f_r = e^{-\Delta/k_B T}$, where $\Delta = E_g^{da} - E_g$, k_B is the Boltzmann constant, and T is the temperature[44] (for details, see the Supplemental Material).

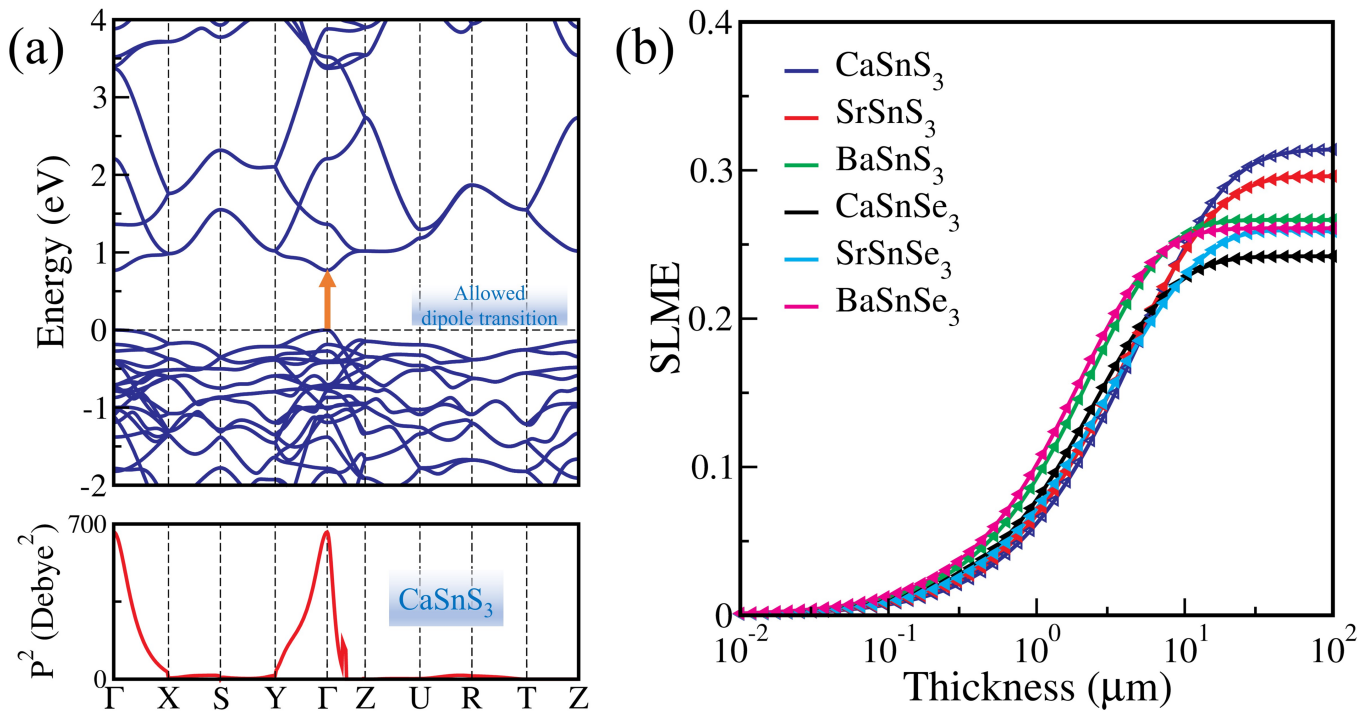


Figure 4. (a) Electronic band structure and transition probability (square of the transition dipole moment matrix elements) of CaSnS_3 calculated using PBE, and (b) spectroscopic limited maximum efficiency (SLME) of ASnX_3 ($A = \text{Ca, Sr, Ba}$; $X = \text{S, Se}$) chalcogenide perovskites calculated using BSE@ G_0W_0 @PBE method.

Next, the thickness dependence of SLME has been computed for all the ASnX_3 ($A = \text{Ca, Sr, Ba}$; $X = \text{S, Se}$) compounds using BSE@ G_0W_0 @PBE method and plotted in Figure 4(b). It is clear that the SLME rises as thickness increases and eventually saturates beyond a certain thickness. The maximum SLME is found to be 31.20% for CaSnS_3 , which is consistent with the previously documented theoretical efficiency of 32.45% at 10 μm thickness[14] and is higher than $\text{CH}_3\text{NH}_3\text{PbI}_3$ (28.97% at 2 μm)[28]. The highest SLME values for SrSnS_3 , BaSnS_3 , CaSnSe_3 , SrSnSe_3 , and BaSnSe_3 compounds are calculated as 29.53%, 26.66%, 24.20%, 25.95%, and 26.09%, respectively. These values of SLME are favorable for the photovoltaic applications compared to transition metal-based traditional CPs and other halide perovskites[14, 15, 22, 78–80] (for details, see Table S14 of the Supplemental Material).

G. Analysis of SCAPS-1D results:

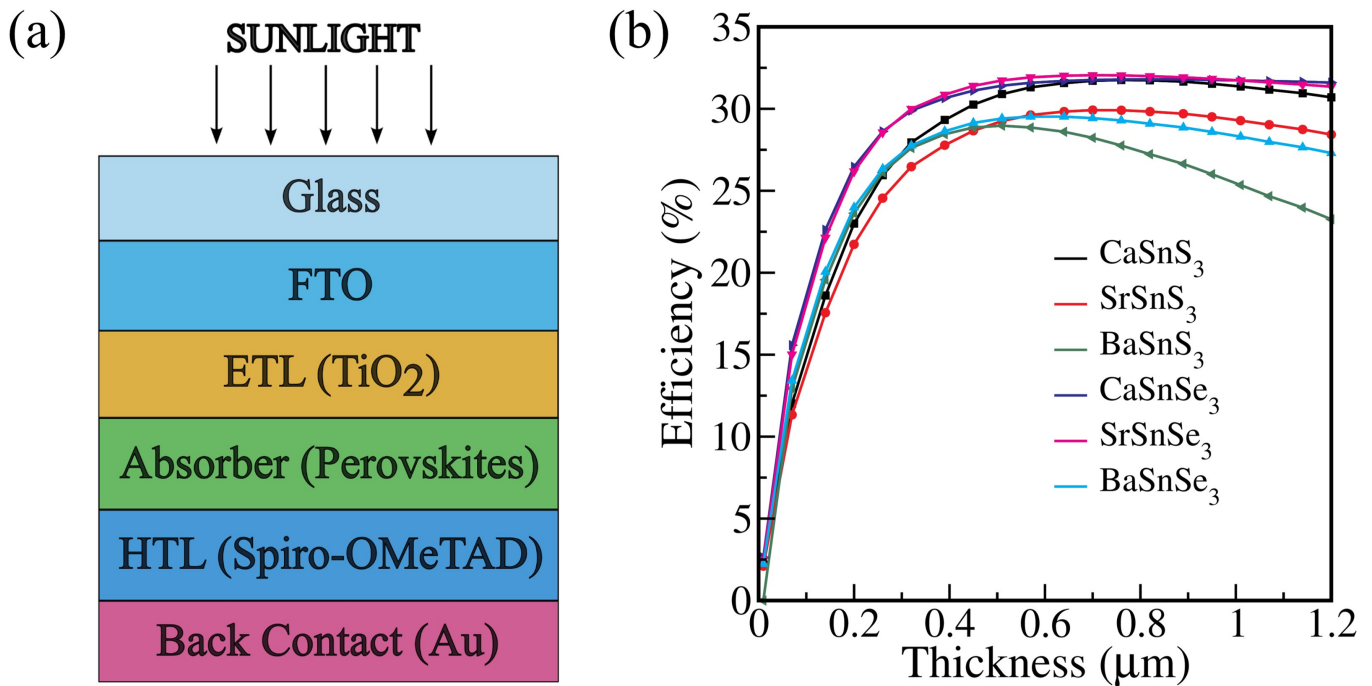


Figure 5. (a) Schematic of the simulated device structure and (b) power conversion efficiency (PCE) of the $ASnX_3$ ($A = Ca, Sr, Ba; X = S, Se$) chalcogenide perovskites-based PSC using SCAPS-1D.

To verify the photovoltaic potential of the investigated systems and our calculated SLME, we also conducted a detailed analysis using the Solar Cell Capacitance Simulator in 1 Dimension (SCAPS-1D). This simulation allowed us to evaluate key performance metrics and gain deeper insights into the efficiency and operational behavior of the devices. Here, the performance of PSC is evaluated by varying the thickness of the absorber layer while keeping the ETL, HTL, and FTO thicknesses constant. The absorber layer thickness is varied from $0.01 \mu\text{m}$ to $1.2 \mu\text{m}$, and it found that the thickness of the perovskite layer has a significant impact on the performance of the PSC [see Figure 5(b)]. After reaching the optimum efficiency, the effect of the thickness of the perovskite layer seems to saturate, which agrees with our SLME calculations. The obtained results are summarized in the Table VII. Our findings indicate that the device simulation results are consistent with the SLME work, specifically for $ASnS_3$ ($A = Ca, Sr, Ba$). On the other hand, the minor discrepancies between the device simulation results for $ASnSe_3$ ($A = Ca, Sr, Ba$) and the SLME findings may be attributed to the materials used in the ETL, HTL, and FTO layers. In our study, SLME provides an idealized efficiency limit based solely on the material's intrinsic optical properties, with its behavior improving for thicker films as absorption approaches a step function, aligning with the SQ limit. However, SCAPS-1D accounts for additional real-world effects, such as carrier transport, recombination losses, and device architecture, which can result in a performance decay for thicker films beyond $1 \mu\text{m}$ due to increased recombination or reduced carrier collection efficiency. This distinction highlights the necessity of combining both methods to achieve a comprehensive assessment of the material's optoelectronic potential, effectively bridging the gap between idealized theoretical predictions and practical device limitations. In general, SCAPS-1D proves to be a highly reliable software, as its simulation results confirm the high efficiency of the investigated materials, closely aligning with theoretical predictions.

Table VII. Photovoltaic parameters of ASnX_3 ($A = \text{Ca, Sr, Ba}$; $X = \text{S, Se}$) chalcogenide perovskites based solar cells using SCAPS-1D.

Optimized Device	V_{oc} (V)	J_{sc} (mA/cm^2)	FF (%)	PCE (%)
FTO/ TiO_2 / CaSnS_3 /Spiro-OMeTAD/Au	1.2885	27.49796	89.63	31.76
FTO/ TiO_2 / SrSnS_3 /Spiro-OMeTAD/Au	1.3239	25.06713	90.15	29.92
FTO/ TiO_2 / BaSnS_3 /Spiro-OMeTAD/Au	0.9871	33.93041	86.49	28.97
FTO/ TiO_2 / CaSnSe_3 /Spiro-OMeTAD/Au	0.7255	55.85582	82.92	31.80
FTO/ TiO_2 / SrSnSe_3 /Spiro-OMeTAD/Au	0.7750	49.34989	83.80	32.05
FTO/ TiO_2 / BaSnSe_3 /Spiro-OMeTAD/Au	0.8050	43.53916	84.22	29.52

Overall, the study of all the above-discussed properties collectively shows that Se-based CaSnSe_3 and SrSnSe_3 demonstrate lower exciton binding energies and higher charge carrier mobilities than the rest of the investigated systems. However, their SLME is also relatively low. On the other hand, S-based CaSnS_3 and SrSnS_3 perovskites exhibit higher SLME despite having higher exciton binding energies and lower charge carrier mobilities compared to the other examined materials. This improved SLME is primarily attributed to the optimal bandgaps of CaSnS_3 and SrSnS_3 compared to their selenium (Se) counterparts, specifically from the perspective of solar cells. This reveals a trade-off between exciton binding energy, charge carrier mobility, and the bandgap of these materials. This suggests that integrating a combination of sulfur (S) and selenium (Se) atoms in these materials could be advantageous for potential application in solar cells, meriting further investigation.

IV. CONCLUSIONS:

In conclusion, we have carried out a comprehensive study to investigate the ground- and excited-state properties of post-transition metal Sn-based distorted chalcogenide perovskites (ASnX_3 ; $A = \text{Ca, Sr, Ba}$, and $X = \text{S, Se}$) under the framework of state-of-the-art DFT combined with DFPT and MBPT (viz., GW and BSE). The mechanical properties confirm the stability, and Pugh's and Poisson's ratios reveal the ductile nature of these perovskites. The bandgaps calculated using G_0W_0 @PBE method are in the range of 0.79–1.50 eV, and the small effective masses of electrons suggest good charge carrier mobility, which is advantageous for energy-harvesting properties. Furthermore, they have a high optical absorption coefficient ($> 10^4 \text{ cm}^{-1}$) and an optical bandgap extending from the near-infrared to the visible range, which is indicated by the BSE calculations. The exciton binding energies of these compounds, ranging from 0.04 to 0.23 eV, are similar to those of transition metal (Zr and Hf) based CPs. Also, these perovskites have smaller carrier-phonon coupling strengths than the conventional lead-based HPs as well as transition metal-based CPs, which leads to better polaron mobility for electrons ($21.33\text{--}416.02 \text{ cm}^2\text{V}^{-1}\text{s}^{-1}$) and holes ($7.02\text{--}260.69 \text{ cm}^2\text{V}^{-1}\text{s}^{-1}$). Additionally, the Fröhlich mesoscopic model implies that the charge-separated polaronic states have lower stability in comparison to bound excitons. Lastly, the SLME method forecasts that one could achieve the highest PCE of up to 31.20% by employing them, which is corroborated by conventional device (FTO/ TiO_2 / ASnX_3 /Spiro-OMeTAD/Au) simulations using SCAPS-1D software. The enhanced properties of Sn-based CPs can be attributed to the distinct valence state of Sn in comparison to transition metal-based CPs. Overall, these results are anticipated to expedite the research and use of chalcogenide perovskites in optoelectronic applications, in general, and solar cell technology, in particular.

ACKNOWLEDGMENTS

The authors would like to acknowledge the Council of Scientific and Industrial Research (CSIR), Government of India [Grant No. 3WS(007)/2023-24/EMR-II/ASPIRE] for financial support. S.A. would also like to acknowledge the CSIR, India [Grant No. 09/1128(11453)/2021-EMR-I] for the Senior Research Fellowship. S. D. thanks Prof. Marc Burgelman, Department of Electronics and Information Systems (ELIS), University of Gent, for providing the SCAPS-1D software. The authors acknowledge the High Performance Computing Cluster (HPCC) 'Magus' at Shiv Nadar Institution of Eminence for providing computational resources that have contributed to the research results reported within this paper.

[1] D. Tiwari, O. S. Hutter, and G. Longo, *J. Phys. Energy* **3**, 034010 (2021).

- [2] S. Niu, H. Huyan, Y. Liu, M. Yeung, K. Ye, L. Blankemeier, T. Orvis, D. Sarkar, D. J. Singh, R. Kapadia, and J. Ravichandran, *Adv. Mater.* **29**, 1604733 (2017), <https://onlinelibrary.wiley.com/doi/pdf/10.1002/adma.201604733>.
- [3] X. Wu, W. Gao, J. Chai, C. Ming, M. Chen, H. Zeng, P. Zhang, S. Zhang, and Y.-Y. Sun, *Sci. China Mater.* **64**, 2976 (2021).
- [4] Y.-Y. Sun, M. L. Agiorgousis, P. Zhang, and S. Zhang, *Nano Lett.* **15**, 581 (2015), <https://doi.org/10.1021/nl504046x>.
- [5] A. Kojima, K. Teshima, Y. Shirai, and T. Miyasaka, *J. Am. Chem. Soc.* **131**, 6050 (2009), <https://doi.org/10.1021/ja809598r>.
- [6] N.-G. Park, *J. Phys. Chem. Lett.* **4**, 2423 (2013), <https://doi.org/10.1021/jz400892a>.
- [7] J. Berry, T. Buonassisi, D. A. Egger, G. Hodes, L. Kronik, Y.-L. Loo, I. Lubomirsky, S. R. Marder, Y. Mastai, J. S. Miller, D. B. Mitzi, Y. Paz, A. M. Rappe, I. Riess, B. Rybtchinski, O. Stafsudd, V. Stevanovic, M. F. Toney, D. Zitoun, A. Kahn, D. Ginley, and D. Cahen, *Adv. Mater.* **27**, 5102 (2015), <https://onlinelibrary.wiley.com/doi/pdf/10.1002/adma.201502294>.
- [8] D. A. Egger, A. M. Rappe, and L. Kronik, *Acc. Chem. Res.* **49**, 573 (2016), <https://doi.org/10.1021/acs.accounts.5b00540>.
- [9] D. B. Straus, S. Guo, A. M. Abeykoon, and R. J. Cava, *Adv. Mater.* **32**, 2001069 (2020), <https://onlinelibrary.wiley.com/doi/pdf/10.1002/adma.202001069>.
- [10] A. Babayigit, A. Ethirajan, M. Muller, and B. Conings, *Nat. Mater.* **15**, 247 (2016).
- [11] A. Swarnkar, W. J. Mir, R. Chakraborty, M. Jagadeeswararao, T. Sheikh, and A. Nag, *Chem. Mater.* **31**, 565 (2019), <https://doi.org/10.1021/acs.chemmater.8b04178>.
- [12] K. V. Sopiha, C. Comparotto, J. A. Marquez, and J. J. S. Scragg, *Adv. Optical Mater.* **10**, 2101704 (2022), <https://onlinelibrary.wiley.com/doi/pdf/10.1002/adom.202101704>.
- [13] K. Kuhar, A. Crovetto, M. Pandey, K. S. Thygesen, B. Seger, P. C. K. Vesborg, O. Hansen, I. Chorkendorff, and K. W. Jacobsen, *Energy Environ. Sci.* **10**, 2579 (2017).
- [14] P. Basera and S. Bhattacharya, *J. Phys. Chem. Lett.* **13**, 6439 (2022), <https://doi.org/10.1021/acs.jpcclett.2c01337>.
- [15] S. Adhikari and P. Johari, *Phys. Rev. B* **109**, 174114 (2024).
- [16] D. Liu, H. Zeng, H. Peng, and R. Sa, *Phys. Chem. Chem. Phys.* **25**, 13755 (2023).
- [17] R. Lelieveld and D. J. W. IJdo, *Acta Cryst. B* **36**, 2223 (1980).
- [18] C.-S. Lee, K. Kleinke, and H. Kleinke, *Solid State Sci.* **7**, 1049 (2005).
- [19] N. A. Moroz, C. Bauer, L. Williams, A. Olvera, J. Casamento, A. A. Page, T. P. Bailey, A. Weiland, S. S. Stoyko, E. Kioupakis, C. Uher, J. A. Aitken, and P. F. P. Poudeu, *Inorg. Chem.* **57**, 7402 (2018), <https://doi.org/10.1021/acs.inorgchem.8b01038>.
- [20] L. J. Tranchitella, B.-H. Chen, J. C. Fettinger, and B. W. Eichhorn, *J. Solid State Chem.* **130**, 20 (1997).
- [21] S. Perera, H. Hui, C. Zhao, H. Xue, F. Sun, C. Deng, N. Gross, C. Milleville, X. Xu, D. F. Watson, B. Weinstein, Y.-Y. Sun, S. Zhang, and H. Zeng, *Nano Energy* **22**, 129 (2016).
- [22] M. Kumar, A. Singh, D. Gill, and S. Bhattacharya, *J. Phys. Chem. Lett.* **12**, 5301 (2021).
- [23] H. M. Ghaithan, S. M. H. Qaid, Z. A. Alahmed, M. Hezam, A. Lyras, M. Amer, and A. S. Aldwayyan, *J. Phys. Chem. C* **125**, 886 (2021), <https://doi.org/10.1021/acs.jpcc.0c07983>.
- [24] R. Comin, G. Walters, E. S. Thibau, O. Voznyy, Z.-H. Lu, and E. H. Sargent, *J. Mater. Chem. C* **3**, 8839 (2015).
- [25] X. Chen, H. Lu, Y. Yang, and M. C. Beard, *J. Phys. Chem. Lett.* **9**, 2595 (2018), PMID: 29714488, <https://doi.org/10.1021/acs.jpcclett.8b00526>.
- [26] J. M. Frost, *Phys. Rev. B* **96**, 195202 (2017).
- [27] Y. Kang and S. Han, *Phys. Rev. Appl.* **10**, 044013 (2018).
- [28] Q. Sun, H. Chen, and W.-J. Yin, *Chem. Mater.* **31**, 244 (2019), <https://doi.org/10.1021/acs.chemmater.8b04320>.
- [29] H. Zou, Y. Duan, S. Yang, D. Xu, L. Yang, J. Cui, H. Zhou, M. Wu, J. Wang, X. Lei, N. Zhang, and Z. Liu, *Small* **19**, 2206205 (2023), <https://onlinelibrary.wiley.com/doi/pdf/10.1002/smll.202206205>.
- [30] R. Guo and S. Wang, *J. Phys. Chem. C* **123**, 29 (2019), <https://doi.org/10.1021/acs.jpcc.8b08041>.
- [31] M.-G. Ju, J. Dai, L. Ma, and X. C. Zeng, *Adv. Energy Mater.* **7**, 1700216 (2017), <https://onlinelibrary.wiley.com/doi/pdf/10.1002/aenm.201700216>.
- [32] H. Shaili, M. Beraich, A. El hat, M. Ouafi, E. mehdi Salmani, R. Essajai, W. Battal, M. Rouchdi, M. Taibi, N. Hassanain, and A. Mzerd, *J. Alloys Compd.* **851**, 156790 (2021).
- [33] P. Hohenberg and W. Kohn, *Phys. Rev.* **136**, B864 (1964).
- [34] W. Kohn and L. J. Sham, *Phys. Rev.* **140**, A1133 (1965).
- [35] M. Gajdoš, K. Hummer, G. Kresse, J. Furthmüller, and F. Bechstedt, *Phys. Rev. B* **73**, 045112 (2006).
- [36] H. Jiang, P. Rinke, and M. Scheffler, *Phys. Rev. B* **86**, 125115 (2012).
- [37] F. Fuchs, C. Rödl, A. Schleife, and F. Bechstedt, *Phys. Rev. B* **78**, 085103 (2008).
- [38] J. P. Perdew, K. Burke, and M. Ernzerhof, *Phys. Rev. Lett.* **77**, 3865 (1996).
- [39] J. Heyd, G. E. Scuseria, and M. Ernzerhof, *J. Chem. Phys.* **118**, 8207 (2003).
- [40] L. Hedin, *Phys. Rev.* **139**, A796 (1965).
- [41] M. S. Hybertsen and S. G. Louie, *Phys. Rev. Lett.* **55**, 1418 (1985).
- [42] S. Albrecht, L. Reining, R. Del Sole, and G. Onida, *Phys. Rev. Lett.* **80**, 4510 (1998).
- [43] M. Röhlfling and S. G. Louie, *Phys. Rev. Lett.* **81**, 2312 (1998).
- [44] L. Yu and A. Zunger, *Phys. Rev. Lett.* **108**, 068701 (2012).
- [45] A. Husainat, W. Ali, P. Cofie, J. Attia, and J. Fuller, *Am. J. Opt. Photonics* **7**, 33 (2019), <https://article.sciencepublishinggroup.com/pdf/10.11648.j.ajop.20190702.12>.
- [46] M. K. Hossain, A. A. Arnab, D. P. Samajdar, M. H. K. Rubel, M. M. Hossain, M. R. Islam, R. C. Das, H. Bencherif, M. F. Rahman, J. Madan, R. Pandey, S. Bhattarai, M. Amami, and D. K. Dwivedi, *Energy Fuels* **37**, 13377 (2023),

<https://doi.org/10.1021/acs.energyfuels.3c02361>.

- [47] S. S. Nishat, M. J. Hossain, F. E. Mullick, A. Kabir, S. Chowdhury, S. Islam, and M. Hossain, *J. Phys. Chem. C* **125**, 13158 (2021), <https://doi.org/10.1021/acs.jpcc.1c02302>.
- [48] S. Ramawat, S. Kukreti, D. J. Sapkota, and A. Dixit, *Energy Fuels* **38**, 9011 (2024), <https://doi.org/10.1021/acs.energyfuels.4c00763>.
- [49] G. Kresse and J. Furthmüller, *Phys. Rev. B* **54**, 11169 (1996).
- [50] G. Kresse and J. Furthmüller, *Comput. Mater. Sci.* **6**, 15 (1996).
- [51] P. E. Blöchl, *Phys. Rev. B* **50**, 17953 (1994).
- [52] K. Momma and F. Izumi, *J. Appl. Crystallogr.* **44**, 1272 (2011).
- [53] A. Togo, L. Chaput, T. Tadano, and I. Tanaka, *J. Phys. Condens. Matter* **35**, 353001 (2023).
- [54] A. M. Ganose, A. J. Jackson, and D. O. Scanlon, *J. Open Source Softw.* **3**, 717 (2018).
- [55] V. Wang, N. Xu, J.-C. Liu, G. Tang, and W.-T. Geng, *Comput. Phys. Commun.* **267**, 108033 (2021).
- [56] S. Adhikari and P. Johari, *Phys. Rev. Mater.* **7**, 075401 (2023).
- [57] M. R. Filip, J. B. Haber, and J. B. Neaton, *Phys. Rev. Lett.* **127**, 067401 (2021).
- [58] R. W. Hellwarth and I. Biaggio, *Phys. Rev. B* **60**, 299 (1999).
- [59] M. Jain, P. Bhumla, M. Kumar, and S. Bhattacharya, *J. Phys. Chem. C* **126**, 6753 (2022), <https://doi.org/10.1021/acs.jpcc.2c00102>.
- [60] R. P. Feynman, *Phys. Rev.* **97**, 660 (1955).
- [61] M. Burgelman, P. Nollet, and S. Degraeve, *Thin Solid Films* **361-362**, 527 (2000).
- [62] M. Burgelman, K. Decock, S. Khelifi, and A. Abass, *Thin Solid Films* **535**, 296 (2013).
- [63] C. Li, X. Lu, W. Ding, L. Feng, Y. Gao, and Z. Guo, *Acta Crystallogr.* **64**, 702 (2008).
- [64] C. J. Bartel, C. Sutton, B. R. Goldsmith, R. Ouyang, C. B. Musgrave, L. M. Ghiringhelli, and M. Scheffler, *Sci. Adv.* **5**, eaav0693 (2019).
- [65] F. Mouhat and F.-X. Coudert, *Phys. Rev. B* **90**, 224104 (2014).
- [66] Z.-j. Wu, E.-j. Zhao, H.-p. Xiang, X.-f. Hao, X.-j. Liu, and J. Meng, *Phys. Rev. B* **76**, 054115 (2007).
- [67] R. Hill, *Proc. Phys. Soc. A* **65**, 349 (1952).
- [68] S. Pugh, London, *Edinburgh Dublin Philos. Mag. J. Sci.* **45**, 823 (1954).
- [69] M. Mattesini, M. Magnuson, F. Tasnádi, C. Höglund, I. A. Abrikosov, and L. Hultman, *Phys. Rev. B* **79**, 125122 (2009).
- [70] X. Liu, B. Xie, C. Duan, Z. Wang, B. Fan, K. Zhang, B. Lin, F. J. M. Colberts, W. Ma, R. A. J. Janssen, F. Huang, and Y. Cao, *J. Mater. Chem. A* **6**, 395 (2018).
- [71] X. Wang, W. Meng, and Y. Yan, *J. Appl. Phys.* **122**, 085104 (2017), <https://doi.org/10.1063/1.4991913>.
- [72] F. Ferreira, A. J. Chaves, N. M. R. Peres, and R. M. Ribeiro, *J. Opt. Soc. Am. B* **36**, 674 (2019).
- [73] S. Adhikari and P. Johari, *Phys. Rev. B* **110**, 014101 (2024).
- [74] M. Bokdam, T. Sander, A. Stroppa, S. Picozzi, D. D. Sarma, C. Franchini, and G. Kresse, *Sci. Rep.* **6**, 28618 (2016).
- [75] C. D. Spataru and F. Leonard, *Chem. Phys.* **413**, 81 (2013).
- [76] H. Fröhlich, *Adv. Phys.* **3**, 325 (1954), <https://doi.org/10.1080/00018735400101213>.
- [77] W. Shockley and H. J. Queisser, *J. Appl. Phys.* **32**, 510 (2004), https://pubs.aip.org/aip/jap/article-pdf/32/3/510/10548356/510_1_online.pdf.
- [78] A. C. Dias, M. P. Lima, and J. L. F. Da Silva, *J. Phys. Chem. C* **125**, 19142 (2021), <https://doi.org/10.1021/acs.jpcc.1c05245>.
- [79] J. Qian, B. Xu, and W. Tian, *Org. Electron.* **37**, 61 (2016).
- [80] J. Kangsanik, V. Sugathan, A. Yadav, A. Yella, and A. Alam, *Phys. Rev. Mater.* **2**, 055401 (2018).